SCIENCE CHINA
Information Sciences

October 2021, Vol. 64 200303:1–200303:15
https://doi.org/10.1007/s11432-020-3253-7

• RESEARCH PAPER •
Special Focus on Reconfigurable Intelligent Surfaces for Future Wireless Communications

Optical true time delay pool-based beamforming and limited feedback for reconfigurable intelligent surface-empowered cloud radio access networks

Huan HUANG[1], Xiaowen WANG[1], Chongfu ZHANG[1,2*], Jie PENG[1], Muchuan YANG[1], Songnian FU[3], Deming LIU[4] & Kun QIU[1]

[1]*School of Information and Communication Engineering, Zhongshan Institute, University of Electronic Science and Technology of China, Chengdu* 611731*, China;*
[2]*School of Electronic Information, University of Electronic Science and Technology of China, Zhongshan Institute, Zhongshan* 528402*, China;*
[3]*School of Information Engineering, Guangdong University of Technology, Guangzhou* 510006*, China;*
[4]*School of Optical and Electronic Information, Huazhong University of Science and Technology, Wuhan* 430074*, China*

Received 30 November 2020/Revised 3 March 2021/Accepted 25 April 2021/Published online 7 September 2021

Abstract Introducing reconfigurable intelligent surfaces (RISs) greatly improves the wireless propagation environment. Limited to feedback overheads and computing power, the low-complexity precoding and the cost-effective beamforming implementation are urgently demanded in RIS-empowered millimeter-wave cloud radio access networks (mmWave C-RANs). Herein, an optical true time delay pool-based hybrid beamforming (OTTDP-based HBF) scheme, enabling centralized analog beamforming control, is proposed for RIS-empowered mmWave C-RANs. By using codebook quantization techniques, we develop a non-iterative limited feedback (NI-LF) precoding algorithm for the RIS-empowered mmWave C-RAN using the proposed OTTDP-based HBF. In the NI-LF precoding algorithm, the complex joint optimization problem of hybrid precoding and phase-shifting of RIS is equivalently formulated as a maximum ratio transmission (MRT) problem and a sparse reconstruction problem. For an active antenna unit (AAU) equipped with eight antennas, a designed example of the proposed OTTDP is presented. Furthermore, for a RIS-empowered mmWave C-RAN at 28 GHz, the received signal-to-noise ratio (SNR) curves obtained via different precoding schemes are compared and discussed. Compared with the precoding without RIS, the proposed NI-LF precoding by using different codebooks to quantize the phase-shifting of the RIS respectively achieves 20.56, 19.55, and 18.93 dB performance improvement for the user located near the 49-element RIS. Moreover, performance degradations due to limited feedback are analyzed. The computational complexity and overhead of the proposed NI-LF precoding algorithm are also given and discussed.

Keywords reconfigurable intelligent surface, optical true time delay, millimeter-wave, cloud radio access network, limited feedback

Citation Huang H, Wang X W, Zhang C F, et al. Optical true time delay pool-based beamforming and limited feedback for reconfigurable intelligent surface-empowered cloud radio access networks. Sci China Inf Sci, 2021, 64(10): 200303, https://doi.org/10.1007/s11432-020-3253-7

1 Introduction

Emerging bandwidth-demanding services such as 4K/8K high-definition video and augmented/virtual reality require significant bandwidth [1]. New radio (NR) standard, including millimeter-wave (mmWave) frequencies, has been launched [2]. mmWave communications spanning a wide frequency range can provide a data rate of Gbps [3,4]. Yet, the excessive path and penetration losses at mmWave frequencies, especially at the frequency of 60 GHz, make the coverage of a mmWave access point (AP) smaller compared with that of a microwave AP [5]. The gain generated from multiple-input multiple-output (MIMO) technologies is essential to compensate for the excessive path and penetration losses at mmWave

* Corresponding author (email: cfzhang@uestc.edu.cn)

frequencies [6,7]. Moreover, to meet the requirement in 5G hot-spot scenarios, plentiful mmWave APs are densely deployed. Cloud radio access networks (C-RANs) provide an attractive approach to connecting these dense mmWave APs [8] and offer several benefits such as high spectral efficiency, low energy consumption [9,10].

In the 5G C-RAN with evolved common public radio interface-based (eCPRI-based) fronthaul[1)], a base station is split into three layers which are the central unit (CU), the distributed unit (DU), and the active antenna unit (AAU). Radio-over-fiber (RoF) technologies are considered to be the most competitive candidates to transmit data between DU and AAU [8]. Generally, RoF can be divided into two categories that are analog RoF (A-RoF) and digital RoF (D-RoF). Compared with D-RoF, A-RoF achieves transparent fronthaul and good optical spectral efficiency [11]. Therefore, A-RoF is more appealing when introducing MIMO into 5G C-RANs [12]. In mmWave communications, based on the perfect channel state information (CSI), hybrid beamforming (HBF) systems can achieve close-to-optimal performance by using a few radio frequency (RF) chains [13,14]. Compared with fully-digital MIMO systems, the HBF systems are easier to implement and more energy-efficient. Besides, HBF significantly improves spectral efficiency through spatial multiplexing compared with analog beamforming [15].

Two approaches to analog beamforming in HBF are achieved by the electrical phase shifter and optical true time delay (OTTD) [16]. Although analog beamforming by using electrical phase shifters is cost-effective, it suffers from beam squint for wideband signals. Optical analog beamforming is not affected by the beam squint issue and also has other advantages, for instance, low energy consumption, low loss, and large bandwidth. Especially, introducing optical analog beamforming into mmWave C-RAN systems allows seamlessly interfacing with the fronthaul networks [8]. Generally, there are two approaches to optical beamforming. One approach to photonic beam steering is achieved by using dispersive media. The common dispersive materials include optical true time delay lines (OTTDLs) [17] and fiber Bragg gratings [18]. The other approach to photonic beam steering is achieved by tuning the wavelength of optical carriers, for instance, using a tunable laser source [19] or selecting appropriate optical carriers from a series of uniformly-spaced optical comb lines [15].

However, supporting mmWave HBF effectively is still a major challenge for mmWave C-RANs [8]. Specifically, in the 5G C-RAN with eCPRI-based fronthaul, the control algorithm for beamforming is assumed to reside in the CU/DU, and analog beamformers or their weight control modules (WCMs) are deployed into all AAUs. In other words, the CSI between AAUs and their service users is fed back to the CU/DU and the precoding for different AAUs is then computed. Feedback on perfect CSI requires lots of feedback overheads, especially for the mmWave C-RAN with plentiful AAUs. Therefore, it is important to design HBF schemes and facilitate the codebook-quantization-based limited feedback for mmWave C-RANs [20–23]. In this case, the CSI is only known at the user and the precoding is then computed. Two widely-used codebooks in practice are the beamsteering (BS) codebook [22,24] and the discrete Fourier transform-based (DFT) beam codebook [25]. Moreover, the traditional physical implementation of a beam codebook is based on the weight control of the antenna array. For both optical and electrical approaches [8,26], the WCMs are generally deployed at the front end of C-RAN systems, i.e., AAUs. Because mmWave AAUs are densely deployed, deploying beamformers or WCMs into each AAU inevitably leads to high operating expenditure and capital expenditure. To this end, we propose centralized beamforming by using optical true time delay pools (OTTDPs) [27,28], where the WCM of analog beamforming for every AP can be physically deployed in the central office. Yet, this centralized beamforming belongs to analog beamforming which cannot obtain the spatial multiplexing gain.

Recently, reconfigurable intelligent surfaces (RISs) as an emerging wireless technology have received considerable attention [29–32]. The RISs consisting of massive passive reflecting elements greatly improve the wireless propagation environment via software-controlled reflection [33]. Therefore, introducing the RISs into mmWave C-RANs with beamforming can further improve the system performance. For a RIS-empowered wireless system, the close-to-optimal performance can be achieved by the alternating optimization (AO) algorithm [34,35]. Yet, in the AO algorithm, the perfect CSI between AAUs and their service users is required, where the fully-digital precoding is also required at the transmitter, i.e., an AAU. Although hybrid precoding has been introduced into RIS-empowered mmWave wireless systems [36,37], the perfect CSI is also required. Limited to fronthaul networks of RIS-empowered mmWave C-RANs [38], the feedback of the perfect CSI is difficult to realize. It is worth noting that some pioneering studies have also considered the imperfect CSI case [39,40]. Besides, the fully-digital precoding and the phase-shifting

1) Common public radio interface: eCPRI interface specification. [2019-05-10]. http://www.cpri.info/downloads/eCPRI_v_2.0_2019_05_10c.pdf.

of RIS are usually obtained by multiple iterations. Because the precoding calculations for all AAUs are completed in the CU/DU, the requirement for computing power in the CU/DU is strict. Therefore, for a RIS-empowered mmWave C-RAN system, the low-complexity precoding with limited feedback is urgently demanded.

In this work, we present an optical true time delay pool-based hybrid beamforming (OTTDP-based HBF) scheme for RIS-empowered mmWave C-RANs. In this OTTDP-based HBF scheme, WCMs of analog beamforming, i.e., the OTTDPs are decoupled from all AAUs and then centralized in the CU/DU. Taking an AAU as an example, the principles and the physical implementation of the proposed OTTDP-based HBF scheme are introduced. Instead of a series of tunable optical filters (TOFs), only a passive wavelength demultiplexer (Demuxer) is employed in each AAU. Because the structure of a mmWave AAU using the OTTDP-based HBF is simple, the dense deployment of mmWave AAUs becomes easy.

To deal with the limitation of feedback overheads and computing power, we develop a non-iterative limited feedback (NI-LF) precoding algorithm for RIS-empowered mmWave C-RANs. In the developed precoding, the codebook used for analog precoding at an AAU is determined by the pre-designed OTTDP and the phase-shift values of RIS are selected from a two-dimension (2D) codebook. Based on the NI-LF precoding, the complex joint optimization problem of hybrid precoding and the phase-shifting of RIS is equivalently formulated as a maximum ratio transmission (MRT) problem and a sparse reconstruction problem. Furthermore, the solutions to the two problems can be respectively computed without iterative. To verify the feasibility of the developed NI-LF precoding algorithm, the results obtained by exploiting a 2D DFT codebook and 2D BS codebooks with different sizes are given and discussed.

Moreover, we employ capital bold type for a matrix e.g., $\boldsymbol{H}_{\mathrm{RU}}$, small bold type for a vector e.g., $\boldsymbol{p}_{\mathrm{w}}$, and italic type for a scalar e.g., M_{A}. The superscripts $(\cdot)^{\mathrm{H}}$, $(\cdot)^{\mathrm{T}}$, and $(\cdot)^{-}$ respectively represent the Hermitian transpose, the transpose, and the generalized inverse of a matrix. The symbol $\|\cdot\|_{\mathrm{F}}$ denotes the Fourier norm.

2 Principles

2.1 Channel model and limited feedback for RIS-empowered C-RANs

In a RIS-empowered mmWave C-RAN, the received signal at the user is composed of signals sent by the serving AAU and RIS, as depicted in Figure 1. We assume that the AAU and the user are equipped with an M_{A}-element uniform linear array (ULA) and M_{U}-element ULA, respectively. Moreover, the RIS modeled as a uniform planar array (UPA) possesses M_{R} reflecting elements. Consider a single-user scenario and the AAU equipped with N_t^{RF} RF chains perform HBF. The received signal can be expressed as [32, 34, 35]

$$\boldsymbol{y} = \boldsymbol{H}_{\mathrm{E}}\boldsymbol{F}_{\mathrm{RF}}^{p}\boldsymbol{F}_{\mathrm{BB}}^{p}\boldsymbol{x} + \boldsymbol{n} = (\boldsymbol{H}_{\mathrm{RU}}\boldsymbol{\Phi}\boldsymbol{H}_{\mathrm{AR}} + \boldsymbol{H}_{\mathrm{AU}})\boldsymbol{F}_{\mathrm{RF}}^{p}\boldsymbol{F}_{\mathrm{BB}}^{p}\boldsymbol{x} + \boldsymbol{n}, \tag{1}$$

where $\boldsymbol{H}_{\mathrm{E}}$ denotes the total channel in the RIS-empowered mmWave C-RAN, $\boldsymbol{H}_{\mathrm{RU}} \in \mathbb{C}^{M_{\mathrm{U}} \times M_{\mathrm{R}}}$ denotes the wireless channel between the RIS and the user termed as the RIS-User channel, $\boldsymbol{H}_{\mathrm{AR}} \in \mathbb{C}^{M_{\mathrm{R}} \times M_{\mathrm{A}}}$ denotes the wireless channel between the AAU and the RIS termed as the AAU-RIS channel, and $\boldsymbol{H}_{\mathrm{AU}} \in \mathbb{C}^{M_{\mathrm{U}} \times M_{\mathrm{A}}}$ denotes the wireless channel between the AAU and the user termed as the AAU-User channel. In (1), $\boldsymbol{F}_{\mathrm{RF}}^{p} \in \mathbb{C}^{M_{\mathrm{A}} \times N_t^{\mathrm{RF}}}$ and $\boldsymbol{F}_{\mathrm{BB}}^{p} \in \mathbb{C}^{N_t^{\mathrm{RF}} \times N_s}$ represent the hybrid analog and digital precoding matrices, and $\boldsymbol{\Phi} \in \mathbb{C}^{M_{\mathrm{R}} \times M_{\mathrm{R}}}$ represents the diagonal phase-shift matrix for the RIS. Moreover, $\boldsymbol{x} \in \mathbb{C}^{N_s \times 1}$ is the symbol vector with N_s data streams and $\boldsymbol{n}$ is the additive white Gaussian noise (AWGN) with zero mean and variance σ^2, i.e., $\boldsymbol{n} \sim \mathcal{CN}(\boldsymbol{0}, \boldsymbol{\sigma^2})$.

The wireless channel at mmWave frequencies can be modeled by the extended Saleh-Valenzuela model [13, 14]. Specifically, the mmWave wireless channels $\boldsymbol{H}_{\mathrm{AU}}$, $\boldsymbol{H}_{\mathrm{AR}}$, and $\boldsymbol{H}_{\mathrm{RU}}$ are written as

$$\boldsymbol{H}_{qp} = \sqrt{\frac{N_q N_p}{\beta^{(i)}(d_{qp}) L_{qp}}} \sum_{l=1}^{L_{qp}} \rho_l^{(i)} \boldsymbol{\alpha}_p(\boldsymbol{\alpha}_q)^{\mathrm{H}}, \tag{2}$$

where $q \in \{\mathrm{A}, \mathrm{R}\}$, $p \in \{\mathrm{R}, \mathrm{U}\}$ and L_{qp} is the number of propagation paths in $\boldsymbol{H}_{qp}$. Moreover, $\rho_l^{(i)} = \rho_l^{(\mathrm{LoS})}$ or $\rho_l^{(\mathrm{NLoS})}$ that denotes the complex gain of the lth line-of-sight (LoS) path or non-line-of-sight (NLoS) path, where $\rho_l^{(\mathrm{LoS})} \sim \mathcal{CN}(0, \sigma_{\mathrm{LoS}})$ and $\rho_l^{(\mathrm{NLoS})} \sim \mathcal{CN}(0, \sigma_{\mathrm{NLoS}})$ [41]. Besides, $\beta^{(i)}(d_{qp}) = \beta^{(\mathrm{LoS})}(d_{qp})$ or

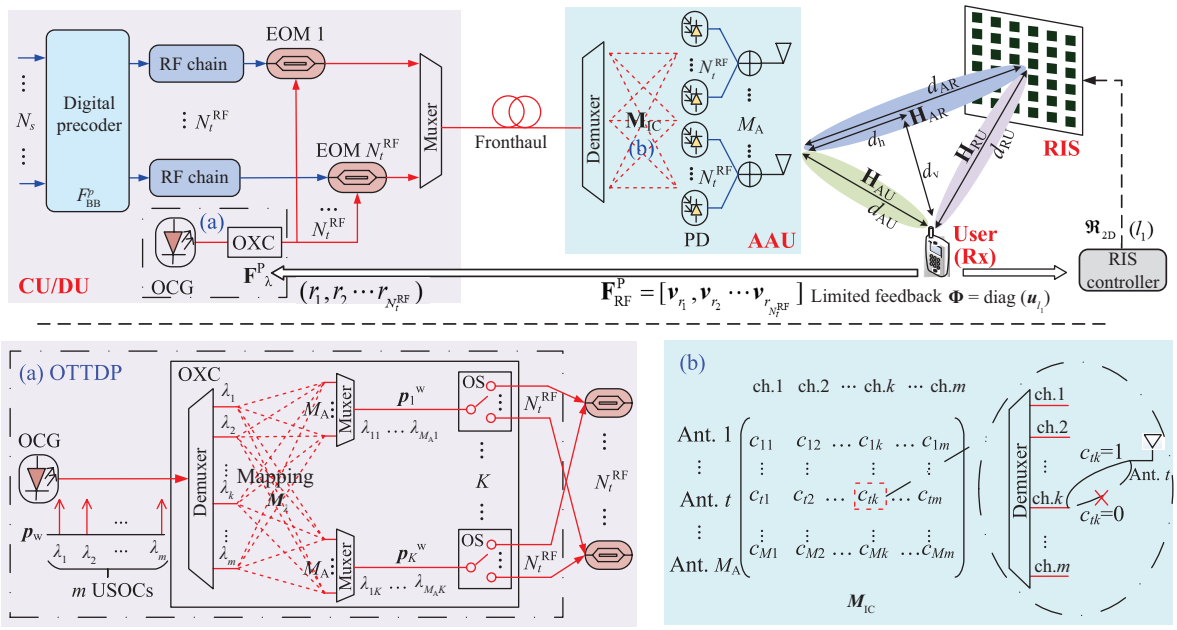

Figure 1 (Color online) Structure of the proposed OTTDP-based HBF and limited feedback for RIS empowered mmWave C-RANs, where (a) physical implementation of the OTTDP and (b) schematic diagram of interconnection matrix $\boldsymbol{M}_{\mathrm{IC}}$ are illustrated.

$\beta^{(\mathrm{NLoS})}(d_{qp})$ that represents the large-scale fading of an LoS or NLoS path, where $d_{qp} \in \{d_{\mathrm{AR}}, d_{\mathrm{AU}}, d_{\mathrm{RU}}\}$ is the distance illustrated in Figure 1. Specifically, the large-scale fading $\beta^{(i)}(d_{qp})$ is expressed as [42]

$$\beta^{(i)}(d_{qp}) = \xi_0 + 10\kappa^{(i)} \log_{10}(d_{qp}) + \varepsilon, \tag{3}$$

where ξ_0 is the least square fit of floating intercept over d_{qp}, and $\kappa^{(i)} = \kappa^{(\mathrm{LoS})}$ or $\kappa^{(\mathrm{NLoS})}$ that is the loss exponent of an LoS or NLoS path. Moreover, ε represents the lognormal shadowing variance.

The array responses $\boldsymbol{\alpha}_p$ and $\boldsymbol{\alpha}_q$ in (2) are only related to the structure of the transmitting and receiving antenna array [14]. For a ULA with M antennas on the y-axis, the array response is given by

$$\boldsymbol{\alpha}(\phi) = \frac{1}{\sqrt{M}} \left[\mathrm{e}^{\mathrm{j}\frac{2\pi}{\lambda_{mm}} d \sin(\phi)(\boldsymbol{\Lambda}(M)-1)} \right]^{\mathrm{T}}, \tag{4}$$

where ϕ is the azimuth angle of arrival, λ_{mm} is the wavelength of transmit mmWave signals, d is the inter-antenna spacing, and $\boldsymbol{\Lambda} = [1, 2, \ldots, M]$. For a UPA with W antennas on the y-axis and H antennas on the z-axis, the array response can be stated as

$$\boldsymbol{\alpha}(\phi, \varphi) = \frac{1}{\sqrt{WH}} \left[\mathrm{e}^{\mathrm{j}\frac{2\pi}{\lambda_{mm}} d((\boldsymbol{\Lambda}(W)-1)\sin(\phi)\sin(\varphi)+(\boldsymbol{\Lambda}(H)-1)\cos(\varphi))} \right]^{\mathrm{T}}, \tag{5}$$

where ϕ and φ are the azimuth and elevation angles of arrival. Specifically, the M_{R}-element RIS can also be modeled as an M_{R}-element UPA, where $M_{\mathrm{R}} = WH$.

For wireless communication systems, an important performance criterion is the received signal-to-noise ratio (SNR) at the user, actually the application of wireless power transfer [32]. According to (1), in the RIS-empowered mmWave C-RAN using HBF, the received SNR can be written as

$$\mathrm{SNR} = \frac{||(\boldsymbol{H}_{\mathrm{RU}} \boldsymbol{\Phi} \boldsymbol{H}_{\mathrm{AR}} + \boldsymbol{H}_{\mathrm{AU}}) \boldsymbol{F}_{\mathrm{RF}}^{p} \boldsymbol{F}_{\mathrm{BB}}^{p}||_{\mathrm{F}}^{2}}{\sigma^2}. \tag{6}$$

Therefore, the optimal precoding matrices $\boldsymbol{F}_{\mathrm{BB}}^{p}$, $\boldsymbol{F}_{\mathrm{RF}}^{p}$, as well as $\boldsymbol{\Phi}$ can be designed by maximizing the received SNR expressed in (6). Generally, introducing mmWave beamforming into the 5G C-RAN with eCPRI-based fronthaul, the control algorithm for beamforming is assumed to reside in the CU/DU, but beamformers or their WCMs are physically implemented in AAUs. Therefore, the beamforming control data must be transmitted from the CU/DU to AAUs, which wastes a lot of fronthaul bandwidth. Moreover, for the RIS-empowered mmWave C-RAN, the optimization of phase-shifting of RISs must be

considered simultaneously. Besides the CSI of $\boldsymbol{H}_{\mathrm{AU}}$, $\boldsymbol{H}_{\mathrm{AR}}$, and $\boldsymbol{H}_{\mathrm{RU}}$ is also required to be known in the CU/DU to compute the optimal precoding matrices. Since the RIS generally comprises a large number of reflecting elements, it brings a great challenge to the uplink fronthaul. To reduce the feedback overhead, a practical way is to perform limited feedback precoding.

For a limited feedback system, the general idea is that the user knows wireless channels and then quantizes precoding matrices by using vector quantization techniques [20]. Naturally, a codebook $\mathfrak{R}$ that is known to both the transmitter and the receiver can be employed to compute the analog precoding matrix. It is worth noting that the dimensions of digital matrices are relatively small compared with that of analog matrices. Moreover, the quantization for the digital matrices has been studied well in the prior work, for instance, the work in [43]. Herein, we focus on the quantization for the analog matrices, i.e., $\boldsymbol{F}_{\mathrm{RF}}^{p}$ and $\boldsymbol{\Phi}$, and the digital precoding matrix $\boldsymbol{F}_{\mathrm{BB}}^{p}$ is assumed to be perfectly fed back. After quantizing, the receiver sends the quantization labels to the transmitter, i.e., the limited feedback. Based on the MRT [44] criterion, the precoding optimization problem in the RIS-empowered mmWave C-RAN with limited feedback and HBF can be stated as

$$\begin{aligned}
&\max_{\boldsymbol{F}_{\mathrm{RF}}^{p},\boldsymbol{F}_{\mathrm{BB}}^{p},\boldsymbol{\Phi}} \ \mathrm{SNR}\\
&\text{s.t. } \boldsymbol{F}_{\mathrm{RF}}^{p}\in\mathfrak{R}_{\mathrm{A}},\\
&\quad \boldsymbol{\varphi}=\left(\mathrm{e}^{\mathrm{j}\varphi_1},\ldots,\mathrm{e}^{\mathrm{j}\varphi_i},\ldots,\mathrm{e}^{\mathrm{j}\varphi_{M_{\mathrm{R}}}}\right)\in\mathfrak{R}_{\mathrm{R}},\\
&\quad 0\leqslant\varphi_i\leqslant 2\pi,\ \forall\, i=1,2,\ldots,M_{\mathrm{R}},\\
&\quad \|\boldsymbol{F}_{\mathrm{RF}}^{p}\boldsymbol{F}_{\mathrm{BB}}^{p}\|_{\mathrm{F}}^{2}\leqslant p_0,
\end{aligned}\tag{7}$$

where $\mathfrak{R}_{\mathrm{A}}$ and $\mathfrak{R}_{\mathrm{R}}$ are the codebooks used for analog precoding at the AAU and the phase-shifting at the RIS, and p_0 denotes maximum transmit power. Moreover, $\boldsymbol{\varphi}$ in (7) is a beamsteering vector belonging to $\mathfrak{R}_{\mathrm{R}}$, where $\boldsymbol{\Phi}=\mathrm{diag}(\boldsymbol{\varphi}^{\mathrm{T}})=\mathrm{diag}(\mathrm{e}^{\mathrm{j}\varphi_1},\mathrm{e}^{\mathrm{j}\varphi_2},\ldots,\mathrm{e}^{\mathrm{j}\varphi_{M_{\mathrm{R}}}})$ and φ_i is the phase-shift value applied by the ith reflecting element of RIS and adjusted by the RIS controller.

2.2 OTTDP-based HBF for RIS-empowered mmWave C-RANs

In the proposed OTTDP-based HBF, the analog beamforming for all AAUs is physically implemented in the CU/DU. Therefore, the control beamforming data do not need to send to each AAU. On the other hand, by using limited feedback, only quantization labels are sent to the CU/DU and the RIS, respectively. Take the implementation of an AAU as an example, Figure 1 schematically shows the OTTDP-based HBF and limited feedback for RIS-empowered mmWave C-RANs.

The pre-designed OTTDP is physically built based on a series of uniformly-spaced optical carriers (USOCs), as depicted in Figure 1(a). These USOCs are generated from an optical comb generator (OCG). Assume that m USOCs are required and the wavelengths of them are termed as $\boldsymbol{p}_{\mathrm{w}}=\{\lambda_i|\lambda_i=\lambda_1+(i-1)\Delta\lambda,\,1\leqslant i\leqslant m\}$, where λ_1 denotes the wavelength of the first USOC, and $\Delta\lambda$ represents the spacing between two adjacent USOCs. Inspired by the codebook-based beamforming [20,21], the limited feedback can be achieved based on a codebook. Therefore, we map $\boldsymbol{p}_{\mathrm{w}}$ to a beam steering matrix $\boldsymbol{M}_{\lambda}$ which is stated as

$$\boldsymbol{M}_{\lambda}=\begin{bmatrix}\lambda_{11} & \lambda_{12} & \cdots & \lambda_{1K}\\ \lambda_{21} & \lambda_{22} & \cdots & \lambda_{K}\\ \vdots & \vdots & \ddots & \vdots\\ \lambda_{M_{\mathrm{A}}1} & \lambda_{M_{\mathrm{A}}2} & \cdots & \lambda_{M_{\mathrm{A}}K}\end{bmatrix}=[\boldsymbol{p}_1^{\mathrm{w}},\boldsymbol{p}_2^{\mathrm{w}},\ldots,\boldsymbol{p}_K^{\mathrm{w}}],\tag{8}$$

where λ_{rh} represents the hth element in the rth row of $\boldsymbol{M}_{\lambda}$ and each element of the $\boldsymbol{M}_{\lambda}$ represents an optical wavelength in the $\boldsymbol{p}_{\mathrm{w}}$. Moreover, the sth column of $\boldsymbol{M}_{\lambda}$ termed as $\boldsymbol{p}_s^{\mathrm{w}}$ is corresponding to a specific beam mode $\boldsymbol{\vartheta}_s$, where the adjacent elements in $\boldsymbol{p}_s^{\mathrm{w}}$ have a fixed difference of $s\Delta\lambda$.

The physical implementation of $\boldsymbol{M}_{\lambda}$ is also shown in Figure 1(a). A passive Demuxer whose channels match $\boldsymbol{p}_{\mathrm{w}}$ is used to separate the m USOCs. These separated USOCs are mapped and then multiplexed by K passive wavelength multiplexers (Muxers). Using an L-km single-mode fiber (SMF) to introduce OTTD, the phase-shift difference $\Delta\varphi_{uv}$ between the u-th and the v-th elements in $\boldsymbol{p}_s^{\mathrm{w}}$ satisfies that

$$\Delta\varphi_{uv}=2\pi f_{mm}(\lambda_{us}-\lambda_{vs})DL=2\pi f_{mm}(u-v)s\Delta\lambda DL,\tag{9}$$

where $f_{mm} = (c/\lambda_{mm})$ denotes the center frequency of the transmit mmWave signals and D represents the dispersion coefficient of the SMF. Note that the L-km SMF can also be used as a fronthaul link, as illustrated in Figure 1. Assuming that the length of the fronthaul link is L_F, the remaining SMF with the length of $(L - L_F)$ can be put into the CU/DU or the AAU. After introducing OTTD, a codebook $\boldsymbol{\mathfrak{R}}_\lambda$ corresponding to $\boldsymbol{M}_\lambda$ is obtained and expressed as

$$\boldsymbol{\mathfrak{R}}_\lambda = \frac{1}{\sqrt{M_{\rm A}}} \begin{bmatrix} 1 & 1 & \cdots & 1 \\ \mathrm{e}^{\mathrm{j}\Delta\varphi} & \mathrm{e}^{\mathrm{j}2\Delta\varphi} & \cdots & \mathrm{e}^{\mathrm{j}K\Delta\varphi} \\ \vdots & \vdots & \ddots & \vdots \\ \mathrm{e}^{\mathrm{j}(M_{\rm A}-1)\Delta\varphi} & \mathrm{e}^{\mathrm{j}(M_{\rm A}-1)2\Delta\varphi} & \cdots & \mathrm{e}^{\mathrm{j}(M_{\rm A}-1)K\Delta\varphi} \end{bmatrix} = [\boldsymbol{v}_1, \boldsymbol{v}_2, \ldots, \boldsymbol{v}_K], \tag{10}$$

where $\Delta\varphi = 2\pi f_{mm}\Delta\lambda DL$.

Note that $\boldsymbol{\mathfrak{R}}_\lambda$ expressed in (10) is also the codebook $\boldsymbol{\mathfrak{R}}_{\rm A}$ in (7), i.e., $\boldsymbol{\mathfrak{R}}_{\rm A} = \boldsymbol{\mathfrak{R}}_\lambda$. By using the $\boldsymbol{v}_s$ as a beam steering vector, beam mode $\boldsymbol{\vartheta}_s$ is then formed at the AAU. The phase-shift values in $\boldsymbol{v}_s$ are achieved by using the USOCs with wavelengths denoted by $\boldsymbol{p}_s^{\rm w}$, where these USOCs are assigned to an RF chain by an optical switch (OS). Furthermore, we define the mapping of $\boldsymbol{M}_\lambda$ and the assignment as the optical cross-connect (OXC) which is illustrated in Figure 1(a).

In the RIS empowered mmWave C-RAN with the OTTDP-based HBF, the limited feedback precoding can be implemented as follows. Firstly, the precoding matrices $\boldsymbol{F}_{\rm BB}^p$, $\boldsymbol{F}_{\rm RF}^p$, as well as $\boldsymbol{\Phi}$ are computed at the user. On the one hand, the analog precoding $\boldsymbol{F}_{\rm RF}^p$ is computed based on the codebook $\boldsymbol{\mathfrak{R}}_\lambda$ expressed by (10). On the other hand, we employ a 2D codebook $\boldsymbol{\mathfrak{R}}_{\rm 2D}$ with M_C codewords for the quantization of $\boldsymbol{\Phi}$, i.e., $\boldsymbol{\mathfrak{R}}_{\rm R} = \boldsymbol{\mathfrak{R}}_{\rm 2D} = [\boldsymbol{u}_1, \boldsymbol{u}_2, \ldots, \boldsymbol{u}_{M_{\rm C}}]$. Moreover, we assume that the RIS modeled as $M_{\rm R}$-element UPA has both W antennas on the y-axis and W antennas on the z-axis, i.e., $M_{\rm R} = W^2$.

Two widely-used codebooks are the DFT codebook and the BS codebook. Specifically, the 2D-DFT codebook $\boldsymbol{\mathfrak{R}}_{\rm DFT}$ can be written as [25]

$$\boldsymbol{\mathfrak{R}}_{\rm DFT} = \left[u_{\rm th}^{\rm DFT}\right]_{t\in\boldsymbol{\Lambda}(M_{\rm R}),h\in\boldsymbol{\Lambda}(M_{\rm R})} = \left[\boldsymbol{u}_1^{\rm DFT}, \boldsymbol{u}_2^{\rm DFT}, \ldots, \boldsymbol{u}_{M_{\rm R}}^{\rm DFT}\right], \tag{11}$$

where the element $u_{\rm th}$ in $\boldsymbol{u}_h^{\rm DFT}$ has the following form that

$$u_{\rm th} = \mathrm{e}^{\mathrm{j}\frac{2\pi}{W}(\mathrm{floor}(\frac{t-1}{W})\times\mathrm{floor}(\frac{h-1}{W})+((h-1)-(\mathrm{floor}(\frac{h-1}{W})\times W))\times((t-1)-(\mathrm{floor}(\frac{t-1}{W})\times W)))}, \tag{12}$$

where $\mathrm{floor}(\cdot)$ represents that rounds the element $\cdot$ to the nearest integer less than or equal to it. Moreover, the 2D BS codebook $\boldsymbol{\mathfrak{R}}_{nm}$ with azimuth and elevation angles of $\frac{2\pi}{2^n}$ and $\frac{\pi}{2^m}$ is built by [22]

$$\boldsymbol{\mathfrak{R}}_{nm} = \left[\sqrt{M_{\rm R}}\boldsymbol{\alpha}\left(\frac{2\,(t-1)\,\pi}{2^n}, \frac{(r-1)\,\pi}{2^m}\right)\right]_{t\in\boldsymbol{\Lambda}(2^n),r\in\boldsymbol{\Lambda}(2^m)} = \left[\boldsymbol{u}_1^{\rm BS}, \boldsymbol{u}_2^{\rm BS}, \ldots, \boldsymbol{u}_{M_{\rm BS}}^{\rm BS}\right], \tag{13}$$

where $\boldsymbol{\alpha}$ is the array response in (5). Note that the number of codewords $M_{\rm BS}$ in the 2D BS codebook $\boldsymbol{\mathfrak{R}}_{nm}$ depends on the quantization accuracy of azimuth and elevation angles, i.e., $M_{\rm BS} = 2^{(n+m)}$.

Secondly, the user feeds back the quantization labels of $\boldsymbol{F}_{\rm RF}^p$, i.e., $(r_1, r_2, \ldots, r_{N_t^{\rm RF}})$ to the CU/DU. Based on the labels, the $N_t^{\rm RF}$ columns are selected from $\boldsymbol{M}_\lambda$ to form the matrix $\boldsymbol{F}_\lambda^p$, i.e., $\boldsymbol{F}_\lambda^p = [\boldsymbol{p}_{r_1}^{\rm w}, \boldsymbol{p}_{r_2}^{\rm w}, \ldots, \boldsymbol{p}_{r_{N_t^{\rm RF}}}^{\rm w}]$. Because USOCs corresponding to $N_t^{\rm RF}$ columns of $\boldsymbol{M}_\lambda$ are used at the same time, a constraint that different elements of $\boldsymbol{M}_\lambda$ cannot be the same is correspondingly imposed on the mapping of $\boldsymbol{M}_\lambda$. Specifically, this constraint is stated as

$$\lambda_{ur} \neq \lambda_{vg} \quad (\forall\lambda_{ur}, \lambda_{vg} \in \boldsymbol{M}_\lambda, u \neq v, r \neq g). \tag{14}$$

Since the pre-designed $\boldsymbol{M}_\lambda$ is mapped from $\boldsymbol{p}_{\rm w}$, the length of $\boldsymbol{p}_{\rm w}$ is desired to be as small as possible. Based on the descriptions thus far, the design of $\boldsymbol{M}_\lambda$ is summarized as

$$\begin{aligned} &\min_m \boldsymbol{p}_{\rm w} = (\lambda_1, \lambda_2, \ldots, \lambda_m) \\ &\text{s.t. } \lambda_{ur} \neq \lambda_{vg} \quad (u \neq v, r \neq g), \\ &\qquad \lambda_{us} - \lambda_{vs} = (u-v)s\Delta\lambda, \quad \forall\lambda_{ur}, \lambda_{vg}, \lambda_{us}, \lambda_{vs} \in \boldsymbol{M}_\lambda. \end{aligned} \tag{15}$$

After the OXC, the USOCs with wavelengths denoted by $\boldsymbol{F}_{\lambda}^{p}$ are selected from the output of the OCG, as depicted in Figure 1. Furthermore, after digital precoding according to $\boldsymbol{F}_{\mathrm{BB}}^{p}$, the N_t^{RF} RF chains are modulated on the selected USOCs by electro-optical modulators (EOMs).

Thirdly, after transmitting through the L-km SMF, the required OTTD is introduced into each RF chain. Instead of a series of TOFs [15], only a passive Demuxer whose channels match the wavelengths denoted as $\boldsymbol{p}_{\mathrm{w}}$ is deployed into each AAU. Thus, introducing the OTTDP-based HBF, the structure of the AAU is very simple. The modulated USOCs are then separated by the Demuxer deployed in the AAU. Therefore, we define an interconnection matrix $\boldsymbol{M}_{\mathrm{IC}} \in \mathbb{R}^{M_{\mathrm{A}} \times m}$ to describe the fixed connection between the M_{A}-element ULA and m channels of the Demuxer, as shown in Figure 1(b).

The $\boldsymbol{M}_{\mathrm{IC}}$ is determined by the beam steering matrix $\boldsymbol{M}_{\lambda}$. The kth element c_{tk} in the tth row of $\boldsymbol{M}_{\lambda}$ is only "1" or "0" that represents the tth antenna (Ant. t) and the kth channel (ch. k) are connected or not. Due to the non-tunability of the passive Demuxer, each column in $\boldsymbol{M}_{\mathrm{IC}}$ contains one element "1" and $(M-1)$ elements "0". Namely, each channel of Demuxer is only connected to one antenna. If a channel is connected to two antennas at the same time, the USOC corresponding to this channel will be assigned to the two antennas, which induces crosstalk. Thus, the constraint that elements in different rows of $\boldsymbol{M}_{\lambda}$ cannot be the same should be satisfied. However, according to (14), this constraint is always satisfied. After detection by photodetectors (PDs), the required phase-shift values are introduced into all RF chains. Namely, the analog precoding is completed. The AAU transmits the mmWave signals.

On the other hand, the user feeds back the quantization labels of the diagonal phase-shift matrix $\boldsymbol{\Phi}$, i.e., (l_1) to the controller of RIS. In other words, the diagonal phase-shift matrix $\boldsymbol{\Phi}$ for the RIS satisfies that $\boldsymbol{\Phi} = \mathrm{diag}(\boldsymbol{u}_{l_1})$.

3 Limited feedback precoding for RIS-empowered mmWave C-RANs

For traditional MIMO systems, some close-to-optimal approaches to solving the precoding optimization problem have been studied, for instance, the MRT. Different from the precoding optimization problem for traditional MIMO systems, the hybrid precoding in RIS-empowered communication systems must consider the influence of introducing RIS. Thus, the hybrid analog and digital precoding matrices $\boldsymbol{F}_{\mathrm{RF}}^{p}$ and $\boldsymbol{F}_{\mathrm{BB}}^{p}$ at the AAU, as well as the phase-shift matrix $\boldsymbol{\Phi}$ at the RIS should be jointly designed.

Consider a general RIS-empowered system, where the transmitter has the availability of fully-digital precoding and knows the perfect CSI [34, 35]. According to the maximum received SNR criterion, the precoding optimization problem for the general RIS-empowered system can be expressed as

$$\begin{aligned} &\max_{\boldsymbol{w},\boldsymbol{\Phi}} \frac{1}{\sigma^2} \left\|(\boldsymbol{H}_{\mathrm{RU}}\boldsymbol{\Phi}\boldsymbol{H}_{\mathrm{AR}} + \boldsymbol{H}_{\mathrm{AU}})\boldsymbol{w}\right\|_{\mathrm{F}}^2 \\ &\text{s.t. } \boldsymbol{\Phi} = \mathrm{diag}\left(\mathrm{e}^{\mathrm{j}\theta_1}, \mathrm{e}^{\mathrm{j}\theta_2}, \ldots, \mathrm{e}^{\mathrm{j}\theta_{M_{\mathrm{R}}}}\right), \\ &\quad 0 \leqslant \theta_i \leqslant 2\pi, \ \forall\, i = 1, 2, \ldots, M_{\mathrm{R}}, \\ &\quad \|\boldsymbol{w}\|_{\mathrm{F}}^2 \leqslant p_0, \end{aligned} \tag{16}$$

where $\boldsymbol{w}$ is the fully-digital precoding at the transmitter. In general, there is no standard method for solving the non-convex problem (16) optimally [34, 35]. Furthermore, the work in [34, 35] has shown that the close-to-optimal solution to the precoding optimization problem in (16) can be computed by the AO algorithm also called the distributed algorithm. The main idea of the AO algorithm is to alternately optimize the fully-digital precoding matrix $\boldsymbol{w}$ and the phase-shift matrix $\boldsymbol{\Phi}$ until the convergence condition is met. Specifically, fix $\boldsymbol{w}$ and compute $\boldsymbol{\Phi}$. According to the obtained $\boldsymbol{\Phi}$, calculate and update $\boldsymbol{w}$. When the convergence condition is satisfied, the close-to-optimal $\boldsymbol{w}$ and $\boldsymbol{\Phi}$ are determined.

Although straightforward methods based on the MRT in the AAU-RIS channel (AAU-RIS-MRT) and the MRT in the AAU-User channels (AAU-User-MRT) have been given in [34, 35], the results based on the straightforward methods without iterative are unsatisfactory. For a single user equipped with one antenna, the solution to the precoding optimization problem expressed by (16) based on AAU-User-MRT is expressed as

$$\begin{aligned} &\boldsymbol{w}_{\mathrm{AU}}^{\mathrm{MRT}} = \sqrt{p_0}\frac{(\boldsymbol{H}_{\mathrm{AU}})^{\mathrm{H}}}{\|\boldsymbol{H}_{\mathrm{AU}}\|_{\mathrm{F}}}, \\ &\theta_i = \angle\left(\boldsymbol{H}_{\mathrm{AU}}\boldsymbol{w}_{\mathrm{AU}}^{\mathrm{MRT}}\right) - \angle\left(\boldsymbol{H}_{\mathrm{RU}}(i)\right) - \angle\left(\boldsymbol{H}_{\mathrm{AR}}(i)\,\boldsymbol{w}_{\mathrm{AU}}^{\mathrm{MRT}}\right), \end{aligned} \tag{17}$$

where $\boldsymbol{H}_{\mathrm{RU}}(i)$ is the ith element of $\boldsymbol{H}_{\mathrm{RU}}$, $\boldsymbol{H}_{\mathrm{AR}}(i)$ is the ith row of $\boldsymbol{H}_{\mathrm{AR}}$, and $\angle(\cdot)$ represents the angle of $(\cdot)$. Note that phase-shift values of the M_{R}-element RIS are computed one by one. Similarly, the solution to (16) based on AAU-RIS-MRT can be stated as

$$\begin{aligned}&\boldsymbol{w}_{\mathrm{AR}}^{\mathrm{MRT}}=\sqrt{p_0}\frac{\left(\boldsymbol{H}_{\mathrm{AR}}(1)\right)^{\mathrm{H}}}{\|\boldsymbol{H}_{\mathrm{AU}}\|_{\mathrm{F}}},\\&\theta_i=\angle\left(\boldsymbol{H}_{\mathrm{AU}}\boldsymbol{w}_{\mathrm{AR}}^{\mathrm{MRT}}\right)-\angle\left(\boldsymbol{H}_{\mathrm{RU}}(i)\right)-\angle\left(\boldsymbol{H}_{\mathrm{AR}}(i)\,\boldsymbol{w}_{\mathrm{AR}}^{\mathrm{MRT}}\right).\end{aligned}\tag{18}$$

When the OTTDP-based HBF is performed for the limited feedback RIS-empowered mmWave C-RAN, the precoding optimization problem in (7) is rewritten as

$$\begin{aligned}\max_{\boldsymbol{F}_{\mathrm{RF}}^{p},\boldsymbol{F}_{\mathrm{BB}}^{p},\boldsymbol{\Phi}}\ &\frac{1}{\sigma^2}\left\|(\boldsymbol{H}_{\mathrm{RU}}\boldsymbol{\Phi}\boldsymbol{H}_{\mathrm{AR}}+\boldsymbol{H}_{\mathrm{AU}})\boldsymbol{F}_{\mathrm{RF}}^{p}\boldsymbol{F}_{\mathrm{BB}}^{p}\right\|_{\mathrm{F}}^{2}\\\text{s.t. }&\boldsymbol{F}_{\mathrm{RF}}^{p}=[\boldsymbol{v}_{r_1},\boldsymbol{v}_{r_2},\ldots,\boldsymbol{v}_{r_{N_t^{\mathrm{RF}}}}]\in\mathfrak{R}_{\lambda},\\&\boldsymbol{\Phi}=\mathrm{diag}(\boldsymbol{u}_{l_1}),\ \boldsymbol{u}_{l_1}\in\mathfrak{R}_{\mathrm{2D}},\\&\left\|\boldsymbol{F}_{\mathrm{RF}}^{p}\boldsymbol{F}_{\mathrm{BB}}^{p}\right\|_{\mathrm{F}}^{2}\leqslant p_0.\end{aligned}\tag{19}$$

First, we assume that the phase-shift matrix $\boldsymbol{\Phi}$ is limited-feedback and the AAU performs the fully-digital precoding $\boldsymbol{w}$. The 2D codebook $\mathfrak{R}_{\mathrm{2D}}$ is employed for computing the phase-shifting of RIS. Specifically, the 2D codebook $\mathfrak{R}_{\mathrm{2D}}$ can be the 2D DFT codebook in (11), the 2D BS codebook in (13), and so on. Correspondingly, the precoding optimization problem expressed in (19) is reduced to

$$\begin{aligned}\max_{\boldsymbol{w},\boldsymbol{\Phi}}\ &\frac{1}{\sigma^2}\left\|(\boldsymbol{H}_{\mathrm{RU}}\boldsymbol{\Phi}\boldsymbol{H}_{\mathrm{AR}}+\boldsymbol{H}_{\mathrm{AU}})\boldsymbol{w}\right\|_{\mathrm{F}}^{2}\\\text{s.t. }&\boldsymbol{\Phi}=\mathrm{diag}\left(\boldsymbol{u}_{l_1}\right),\ \boldsymbol{u}_{l_1}\in\mathfrak{R}_{\mathrm{2D}},\\&\|\boldsymbol{w}\|_{\mathrm{F}}^{2}\leqslant p_0.\end{aligned}\tag{20}$$

For any given phase-shift matrix $\boldsymbol{\Phi}$, the precoding optimization problem expressed in (20) can be rewritten as

$$\begin{aligned}\max_{\boldsymbol{w}}\ &\frac{1}{\sigma^2}\left\|\boldsymbol{H}_{\mathrm{E}}\boldsymbol{w}\right\|_{\mathrm{F}}^{2}\\\text{s.t. }&\|\boldsymbol{w}\|_{\mathrm{F}}^{2}\leqslant p_0.\end{aligned}\tag{21}$$

Because $\boldsymbol{H}_{\mathrm{E}}=(\boldsymbol{H}_{\mathrm{RU}}\boldsymbol{\Phi}\boldsymbol{H}_{\mathrm{AR}}+\boldsymbol{H}_{\mathrm{AU}})$ in (21) is fixed, the problem (21) is a typical MIMO precoding optimization problem. Inspired by the work in [34, 44], the solution to (21) can be computed by

$$\boldsymbol{w}=\sqrt{p_0}\frac{\boldsymbol{H}_{\mathrm{E}}^{\mathrm{H}}}{\|\boldsymbol{H}_{\mathrm{E}}\|_{\mathrm{F}}}.\tag{22}$$

For the certain $\boldsymbol{\Phi}$, therefore, the maximum received SNR is equal to $\frac{p_0\|\boldsymbol{H}_{\mathrm{E}}\|_{\mathrm{F}}^2}{\sigma^2}$. Because $\boldsymbol{H}_{\mathrm{E}}$ can be modified by $\boldsymbol{\Phi}$, the optimal phase-shift matrix $\boldsymbol{\Phi}_{\mathrm{opt}}$ is determined by

$$\begin{aligned}&\boldsymbol{\Phi}_{\mathrm{opt}}=\arg\max\left(\|\boldsymbol{H}_{\mathrm{E}}\|_{\mathrm{F}}^{2}\right)=\arg\max\left(\|(\boldsymbol{H}_{\mathrm{RU}}\boldsymbol{\Phi}\boldsymbol{H}_{\mathrm{AR}}+\boldsymbol{H}_{\mathrm{AU}})\|_{\mathrm{F}}^{2}\right)\\&\text{s.t. }\boldsymbol{\Phi}_{\mathrm{opt}}=\mathrm{diag}\left(\boldsymbol{u}_{l_1}\right),\ \boldsymbol{u}_{l_1}\in\mathfrak{R}_{\mathrm{2D}}.\end{aligned}\tag{23}$$

The optimal phase-shift matrix $\boldsymbol{\Phi}_{\mathrm{opt}}$ can be obtained by (23). Note that the solution to $\boldsymbol{\Phi}_{\mathrm{opt}}$ expressed as (23) represents the processes of selecting the maximum beamforming gain codeword $\boldsymbol{u}_{l_1}$ from $\mathfrak{R}_{\mathrm{2D}}$. Specifically, this codeword selection can be finished by a selection-based protocol [3]. Unlike the work in [34, 35], all phase-shift values of M_{R}-element RIS are determined at the same time, i.e., $(\mathrm{e}^{\mathrm{j}\theta_1}, \mathrm{e}^{\mathrm{j}\theta_2},\ldots,\mathrm{e}^{\mathrm{j}\theta_{M_{\mathrm{R}}}})=\boldsymbol{u}_{l_1}$. It is worth noting that only the CSI of the combined channel $(\boldsymbol{H}_{\mathrm{RU}}\mathrm{diag}(\boldsymbol{u}_{l_1})\boldsymbol{H}_{\mathrm{AR}}+\boldsymbol{H}_{\mathrm{AU}})$ is required to be perfectly known to the user. After selecting $\boldsymbol{u}_{l_1}$ by the selection-based protocol, the CSI of the combined channel can be obtained at the user by channel estimation [45] or pilot training [46].

For the optimal phase-shift matrix $\boldsymbol{\Phi}_{\mathrm{opt}}$, the optimal fully-digital precoding can be computed by (22), i.e., $\boldsymbol{w}_{\mathrm{opt}}=\frac{\sqrt{p_0}(\boldsymbol{H}_{\mathrm{RU}}\mathrm{diag}(\boldsymbol{u}_{l_1})\boldsymbol{H}_{\mathrm{AR}}+\boldsymbol{H}_{\mathrm{AU}})^{\mathrm{H}}}{\|(\boldsymbol{H}_{\mathrm{RU}}\mathrm{diag}(\boldsymbol{u}_{l_1})\boldsymbol{H}_{\mathrm{AR}}+\boldsymbol{H}_{\mathrm{AU}})\|_{\mathrm{F}}}$.

Therefore, by using the limited feedback on the phase-shift matrix $\boldsymbol{\Phi}$, the complex joint optimization problem of $\boldsymbol{w}$ and $\boldsymbol{\Phi}$ can be computed without an iterative process. Inspired by the original work in [14], the hybrid analog and digital precoding matrices $\boldsymbol{F}_{\mathrm{RF}}^{p}$ and $\boldsymbol{F}_{\mathrm{BB}}^{p}$ in (18) can be obtained by solving

$$\begin{aligned}&\min_{\boldsymbol{F}_{\mathrm{RF}}^{p},\boldsymbol{F}_{\mathrm{BB}}^{p}} \|\boldsymbol{w}_{\mathrm{opt}}-\boldsymbol{F}_{\mathrm{RF}}^{p}\boldsymbol{F}_{\mathrm{BB}}^{p}\|_{\mathrm{F}}^{2}\\ &\text{s.t. } \boldsymbol{F}_{\mathrm{RF}}^{p}=[\boldsymbol{v}_{r_1},\boldsymbol{v}_{r_2},\ldots,\boldsymbol{v}_{r_{N_t^{\mathrm{RF}}}}]\in\mathfrak{R}_{\lambda},\\ &\quad \|\boldsymbol{F}_{\mathrm{RF}}^{p}\boldsymbol{F}_{\mathrm{BB}}^{p}\|_{\mathrm{F}}^{2}\leqslant p_0.\end{aligned}\tag{24}$$

Based on the discussion so far, the complex joint optimization problem of $\boldsymbol{F}_{\mathrm{RF}}^{p}$, $\boldsymbol{F}_{\mathrm{BB}}^{p}$, as well as $\boldsymbol{\Phi}$ can be solved by computing (22) and (24), respectively. Moreover, the pseudo-code for the NI-LF precoding solution is given in Algorithm 1. The solution to (24) can also be found in Algorithm 1, i.e., the for loop.

Algorithm 1 NI-LF precoding for RIS-empowered mmWave C-RANs

Given: $\boldsymbol{H}_{\mathrm{AU}}$, $\boldsymbol{H}_{\mathrm{AR}}$, $\boldsymbol{H}_{\mathrm{RU}}$, $\mathfrak{R}_{\lambda}$, $\mathfrak{R}_{\mathrm{2D}}$, and p_0;
Initialize: $\boldsymbol{F}_{\mathrm{RF}}^{p}=\boldsymbol{0}_{M_{\mathrm{A}}\times N_t^{\mathrm{RF}}}$ and $\boldsymbol{F}_{\mathrm{BB}}^{p}=\boldsymbol{0}_{N_t^{\mathrm{RF}}\times N_s}$;
Select the maximum beamforming gain codeword $\boldsymbol{u}_{l_1}$ from $\mathfrak{R}_{\mathrm{2D}}$;
Calculate $\boldsymbol{w}_{\mathrm{opt}}=\frac{\sqrt{p_0}(\boldsymbol{H}_{\mathrm{RU}}\mathrm{diag}(\boldsymbol{u}_{l_1})\boldsymbol{H}_{\mathrm{AR}}+\boldsymbol{H}_{\mathrm{AU}})^{\mathrm{H}}}{\|(\boldsymbol{H}_{\mathrm{RU}}\mathrm{diag}(\boldsymbol{u}_{l_1})\boldsymbol{H}_{\mathrm{AR}}+\boldsymbol{H}_{\mathrm{AU}})\|_{\mathrm{F}}}$ and let $\boldsymbol{F}_{\mathrm{res}}=\boldsymbol{w}_{\mathrm{opt}}$;
for $i=1\rightarrow N_t^{\mathrm{RF}}$ **do**
  Find $\boldsymbol{v}_t$ from $\mathfrak{R}_{\lambda}$ by $t=\arg\max_{p\in[1\cdots K]}|\langle\boldsymbol{v}_p,\boldsymbol{F}_{\mathrm{res}}\rangle|$, $\boldsymbol{v}_p\in\mathfrak{R}_{\lambda}$;
  Update $\boldsymbol{F}_{\mathrm{RF}}^{p}$ via $\boldsymbol{F}_{\mathrm{RF}}^{p}=\boldsymbol{F}_{\mathrm{RF}}^{p}\bigcup\boldsymbol{v}_t$;
  Compute $\boldsymbol{F}_{\mathrm{BB}}^{p}$ by $\boldsymbol{F}_{\mathrm{BB}}^{p}=((\boldsymbol{F}_{\mathrm{RF}}^{p})^{\mathrm{H}}\boldsymbol{F}_{\mathrm{RF}}^{p})^{-}(\boldsymbol{F}_{\mathrm{RF}}^{p})^{\mathrm{H}}\boldsymbol{w}_{\mathrm{opt}}$;
  Update $\boldsymbol{F}_{\mathrm{res}}$ by $\boldsymbol{F}_{\mathrm{res}}=\frac{\boldsymbol{w}_{\mathrm{opt}}-\boldsymbol{F}_{\mathrm{RF}}^{p}\boldsymbol{F}_{\mathrm{BB}}^{p}}{\|\boldsymbol{w}_{\mathrm{opt}}-\boldsymbol{F}_{\mathrm{RF}}^{p}\boldsymbol{F}_{\mathrm{BB}}^{p}\|_{\mathrm{F}}}$;
  Satisfy the transmit power constraint by $\boldsymbol{F}_{\mathrm{BB}}^{p}=\frac{\sqrt{p_0}\boldsymbol{F}_{\mathrm{BB}}^{p}}{\|\boldsymbol{F}_{\mathrm{RF}}^{p}\boldsymbol{F}_{\mathrm{BB}}^{p}\|_{\mathrm{F}}}$;
end for
Send the labels $(r_1,r_2,\ldots,r_{N_t^{RF}})$ to the CU/DU;
Send the label (l_1) to the RIS controller.

The computational complexity and overheads of the proposed NI-LF precoding algorithm and the AO algorithm are shown in Table 1. The computational complexity is provided according to the required numbers of complex multiplications and divisions. Because $\boldsymbol{w}_{\mathrm{opt}}$ in Algorithm 1 is directly obtained based on the combined channel, it requires no computational complexity. Therefore, the proposed NI-LF precoding algorithm approximately requires $\mathcal{O}(N_t^{\mathrm{RF}}(K+M_{\mathrm{A}}(2K+(N_t^{\mathrm{RF}})^2+3N_t^{\mathrm{RF}}+2)))$ times of multiplications and $\mathcal{O}(N_t^{\mathrm{RF}}(N_t^{\mathrm{RF}}+1)(2N_t^{\mathrm{RF}}+1)/6)$ times of divisions. For comparison, the corresponding results of the AO algorithm are computed. Assuming that the number of iterations is κ, the AO algorithm requires $\mathcal{O}(\kappa(3M_{\mathrm{R}}^2+5M_{\mathrm{R}}M_{\mathrm{A}}+2M_{\mathrm{A}}))$ times of multiplications and no divisions. Generally, the RIS comprises plentiful reflecting elements, i.e., $M_{\mathrm{R}}\gg M_{\mathrm{A}}\geqslant N_t^{\mathrm{RF}}\geqslant N_s$.

For the AO algorithm, the authors [35] assumed that the CSI of all channels has been perfectly known at the transmitter. Therefore, the training overhead of the required CSI is positively related to the sizes of $\boldsymbol{H}_{\mathrm{RU}}$, $\boldsymbol{H}_{\mathrm{AR}}$, and $\boldsymbol{H}_{\mathrm{AU}}$, i.e., $M_{\mathrm{U}}\times M_{\mathrm{R}}$, $M_{\mathrm{R}}\times M_{\mathrm{A}}$, and, $M_{\mathrm{U}}\times M_{\mathrm{A}}$. Specifically, using analog-to-digital converters with B-bit precision to quantify the required CSI, the training overhead required in the AO algorithm is equal to $(M_{\mathrm{U}}\times M_{\mathrm{R}}+M_{\mathrm{R}}\times M_{\mathrm{A}}+M_{\mathrm{U}}\times M_{\mathrm{A}})\times B$ bits. However, only the CSI of the combined channel $(\boldsymbol{H}_{\mathrm{RU}}\mathrm{diag}\,(\boldsymbol{u}_{l_1})\boldsymbol{H}_{\mathrm{AR}}+\boldsymbol{H}_{\mathrm{AU}})$ is required in the proposed algorithm. In other words, the training overhead in the proposed algorithm is related to the sizes of the combined channel, i.e., $M_{\mathrm{U}}\times M_{\mathrm{A}}$. Therefore, the training overhead in the proposed algorithm is equal to $(M_{\mathrm{U}}\times M_{\mathrm{A}}\times B)$ bits. Moreover, the phase-shift values $(\mathrm{e}^{\mathrm{j}\theta_1},\mathrm{e}^{\mathrm{j}\theta_2},\ldots,\mathrm{e}^{\mathrm{j}\theta_{M_{\mathrm{R}}}})$ should be sent to the RIS controller, and thus the feedback overhead required in the AO algorithm is equal to $(M_{\mathrm{R}}\times B)$ bits. In the proposed NI-LF precoding algorithm, the digital precoding matrix $\boldsymbol{F}_{\mathrm{BB}}^{p}\in\mathbb{C}^{N_t^{\mathrm{RF}}\times N_s}$ and the quantization labels $(r_1,r_2,\ldots,r_{N_t^{\mathrm{RF}}})$ of the analog precoding matrix $\boldsymbol{F}_{\mathrm{RF}}^{p}$ are needed to be fed back. Consequently, the feedback overhead required in the proposed NI-LF precoding algorithm is $(N_s\times N_t^{\mathrm{RF}}\times B+N_t^{\mathrm{RF}}\times B_{\lambda})$ bits, where B_{λ} is determined by K that satisfies $2^{(B_{\lambda}-1)}<K\leqslant 2^{B_{\lambda}}$ and K is the number of codewords in $\mathfrak{R}_{\lambda}$.

Table 1 The complexity and overheads of the proposed NI-LF precoding and AO algorithms

	The AO algorithm	The proposed NI-LF precoding algorithm
Number of multiplications	$\mathcal{O}(\kappa(3M_{\mathrm{R}}^2+5M_{\mathrm{R}}M_{\mathrm{A}}+2M_{\mathrm{A}}))$	$\mathcal{O}(N_t^{\mathrm{RF}}(K+M_{\mathrm{A}}(2K+(N_t^{\mathrm{RF}})^2+3N_t^{\mathrm{RF}}+2)))$
Number of divisions	–	$\mathcal{O}(N_t^{\mathrm{RF}}(N_t^{\mathrm{RF}}+1)(2N_t^{\mathrm{RF}}+1)/6)$
Training overhead	$(M_{\mathrm{U}}\times M_{\mathrm{R}}+M_{\mathrm{R}}\times M_{\mathrm{A}}+M_{\mathrm{U}}\times M_{\mathrm{A}})\times B$	$(M_{\mathrm{U}}\times M_{\mathrm{A}})\times B$
Feedback overhead	$M_{\mathrm{R}}\times B$	$N_s\times N_t^{\mathrm{RF}}\times B+N_t^{\mathrm{RF}}\times B_\lambda$

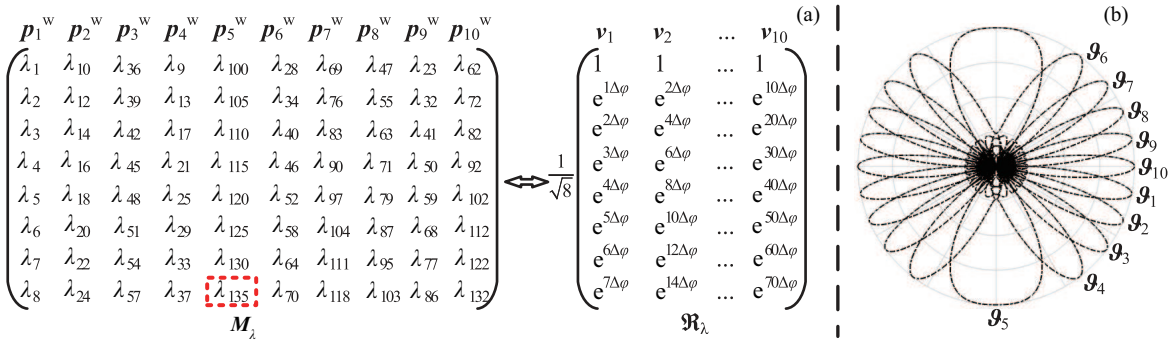

Figure 2 (Color online) (a) An example of the 8×10 beam steering matrix $\boldsymbol{M}_\lambda$ and its corresponding codebook $\boldsymbol{\mathfrak{R}}_\lambda$, and (b) beam modes corresponding to $\boldsymbol{\mathfrak{R}}_\lambda$.

4 Designed example and result discussion

Consider a RIS-empowered mmWave C-RAN at 28 GHz, where the AAU is equipped with an eight-elements ULA modeled by (4) and three RF chains, i.e., $M_{\mathrm{A}}=8$ and $N_t^{\mathrm{RF}}=3$. Moreover, we assume that the user possesses a single antenna, i.e., $M_{\mathrm{U}}=1$. The RIS comprising 49 reflecting elements is modeled as a 49-element UPA with $W=H=7$, i.e., $M_{\mathrm{R}}=49$. In the proposed OTTDP-based HBF, the number of beam modes in $\boldsymbol{\mathfrak{R}}_\lambda$ is set to be 10, i.e., $K=10$. Furthermore, the corresponding $\boldsymbol{M}_\lambda$ illustrated in Figure 2(a) is obtained via (14). Because only a passive Demuxer is deployed in the AAU, the structure of the AAU is low-cost and low-complexity.

According to the quantization labels of $\boldsymbol{F}_{\mathrm{RF}}^p$, the wavelength matrix $\boldsymbol{F}_\lambda^p$ is determined. The USOCs with wavelengths corresponding to $\boldsymbol{F}_\lambda^p$ are then selected after OXC. Specifically, assuming that $\boldsymbol{F}_\lambda^p=[\boldsymbol{p}_1^{\mathrm{w}},\boldsymbol{p}_2^{\mathrm{w}},\boldsymbol{p}_3^{\mathrm{w}}]$, these M_{A} USOCs with wavelengths corresponding to $\boldsymbol{p}_1^{\mathrm{w}}$ are selected and then the first RF chain is modulated on them. Similarly, the USOCs with wavelengths corresponding to $\boldsymbol{p}_2^{\mathrm{w}}$ and $\boldsymbol{p}_3^{\mathrm{w}}$ are used to introduce OTTD into the second and the third RF chains. After introducing OTTD by the SMF and detecting by PDs, the required phase shift is introduced. Moreover, all beam modes corresponding to $\boldsymbol{M}_\lambda$ are depicted in Figure 2(b).

For traceability of the analysis, we also assume that the user always lies on the horizontal line parallel to that between the AAU and the RIS [34,37]. Furthermore, we set the vertical distance d_{v} illustrated in Figure 1 to be 2 m. The horizontal distance d_{h} is then defined as $d_{\mathrm{h}}^2=d_{\mathrm{AU}}^2-d_{\mathrm{v}}^2$. Moreover, the RIS is assumed to be deployed at a location 45 m away from the AAU, i.e., $d_{\mathrm{AR}}=45$ m. We consider a practical scenario that propagation paths between the AAU and the user are the NLoS paths so the RIS is introduced to proactively modify the unexpected propagation environment. The numbers of propagation paths in $\boldsymbol{H}_{\mathrm{AU}}$, $\boldsymbol{H}_{\mathrm{AR}}$, and $\boldsymbol{H}_{\mathrm{RU}}$ are set to be three, i.e., $L_{\mathrm{AU}}=L_{\mathrm{AR}}=L_{\mathrm{RU}}=3$. Other simulation parameters in the channel models are stated as follows: $\sigma^2=-110$ dBm, $\xi_0=61.4$ dB, $\kappa^{(\mathrm{LoS})}=2$, $\kappa^{(\mathrm{NLoS})}=5$, $\varepsilon\sim\mathcal{N}(0,5.8)$, $\rho_l^{(\mathrm{LoS})}\sim\mathcal{CN}(0,1)$, and $\rho_l^{(\mathrm{NLoS})}\sim\mathcal{CN}(0,0.1)$. Then the mmWave wireless channels $\boldsymbol{H}_{\mathrm{AU}}$, $\boldsymbol{H}_{\mathrm{AR}}$, and $\boldsymbol{H}_{\mathrm{RU}}$ are built by (2). Moreover, p_0 in Algorithm 1 is equal to 30 dBm.

Based on different precoding schemes, the logarithmic received SNR ($10\log_{10}\mathrm{SNR}$) versus the horizontal distance d_{h} is shown in Figure 3, where all results are obtained from 2000 trials. As an upper limit of the received SNR, the received SNR curve obtained via the AO algorithm [34,35] is given in Figure 3 by plus signs, where the AAU performs fully-digital precoding (AO & FP).

On the one hand, the received SNR curves obtained based on the proposed NI-LF precoding are illustrated in Figure 3, where the phase-shifting of RIS quantified by the 2D BS codebook $\boldsymbol{\mathfrak{R}}_{54}$ (NI-LF w/ $\boldsymbol{\mathfrak{R}}_{54}$), the 2D DFT codebook $\boldsymbol{\mathfrak{R}}_{\mathrm{DFT}}$ (NI-LF w/ $\boldsymbol{\mathfrak{R}}_{\mathrm{DFT}}$), the 2D BS codebook $\boldsymbol{\mathfrak{R}}_{43}$ (NI-LF w/ $\boldsymbol{\mathfrak{R}}_{43}$) is respectively marked by squares, circles, and downward-pointing triangles. Note that the codebook $\boldsymbol{\mathfrak{R}}_\lambda$

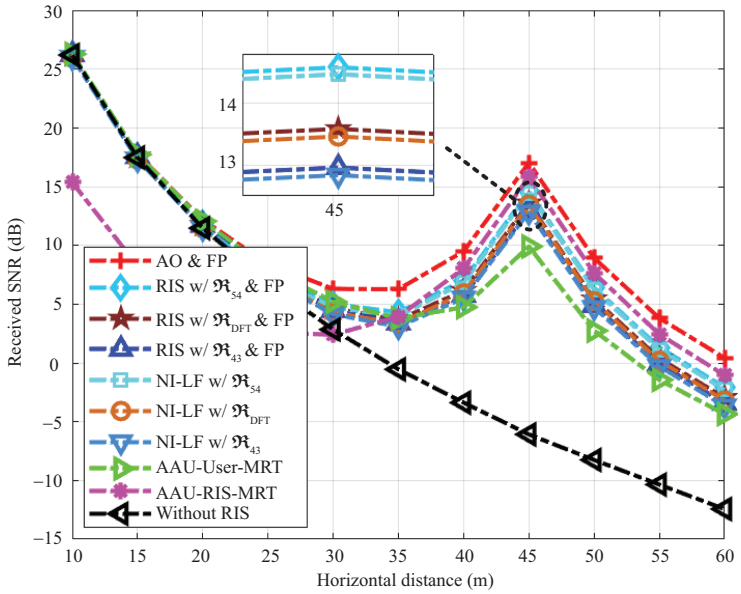

Figure 3 (Color online) Received SNR versus horizontal distance based on different schemes.

used in NI-LF w/ $\mathfrak{R}_{54}$, NI-LF w/ $\mathfrak{R}_{\mathrm{DFT}}$, and NI-LF w/ $\mathfrak{R}_{43}$ is shown in Figure 2. On the other hand, we assume that the codebook-quantization-based (CQ-based) phase-shifting is obtained by $\mathfrak{R}_{54}$, $\mathfrak{R}_{\mathrm{DFT}}$, and $\mathfrak{R}_{43}$, but the AAU performs fully-digital precoding. Correspondingly, the received SNR curves via RIS w/ $\mathfrak{R}_{54}$ & FP, RIS w/ $\mathfrak{R}_{\mathrm{DFT}}$ & FP, and RIS w/ $\mathfrak{R}_{43}$ & FP are depicted in Figure 3 by diamonds, pentagrams, and upward-pointing triangles.

Moreover, the received SNR curves obtained by AAU-User-MRT and AAU-RIS-MRT are shown in Figure 3 by right-pointing triangles and asterisks. As a comparison with the received SNR curves of RIS-empowered mmWave C-RANs, the received SNR based on fully-digital precoding without the RIS is also given and plotted by left-pointing triangles. Specifically, the received SNR without the RIS is computed via (21), where $\boldsymbol{H}_{\mathrm{E}} = \boldsymbol{H}_{\mathrm{AU}}$.

When the user is close to the AAU ($d_{\mathrm{h}} < 30$ m), the received SNR is mainly determined by the AAU-User channel. Because the user is far away from the location of the RIS, the improvement generated from the RIS is slight. Therefore, the received SNR by using the RIS is similar to that without the RIS. Meanwhile, the performance based on AAU-RIS-MRT is poor. When the user gets close to the RIS ($d_{\mathrm{h}} > 30$ m), the received SNR is greatly improved by introducing the RIS while the performance based on AAU-User-MRT deteriorates. In other words, the received signal component assisted by the RIS plays a dominant role in the received SNR. Because the distance between the RIS and the AAU is 45 m, the user at $d_{\mathrm{h}} = 45$ m gets maximum gain from the RIS. Consequently, we can see a spike at 45 m in Figure 3. As illustrated in Figure 3, about 20.56, 19.55, and 18.93 dB performance improvement can be respectively achieved via NI-LF w/ $\mathfrak{R}_{54}$, NI-LF w/ $\mathfrak{R}_{\mathrm{DFT}}$, and NI-LF w/ $\mathfrak{R}_{43}$. Although better performance can be achieved by increasing the accuracy of the azimuth and elevation angles in the 2D BS codebook $\mathfrak{R}_{nm}$, a more precise RIS controller is required and the maximum beamforming gain codeword $\boldsymbol{u}_{l_1}$ selected from $\mathfrak{R}_{\mathrm{2D}}$ also takes more time.

Compared with that based on CQ-based phase-shifting and FP, the received SNR achieved by CQ-based phase-shifting and OTTDP-based HBF is slightly reduced. Based on the proposed OTTDP-based HBF scheme, however, only three RF chains are required and three quantization labels of analog precoding, i.e., (r_1, r_2, r_3) are fed back to the CU/DU. In the RIS-empowered mmWave C-RAN with the OTTDP-based HBF, the physical implementation and the control of analog precoding for different AAUs are centralized at the CU/DU, where we only employ a passive Demuxer instead of expensive TOFs at each AAU. Therefore, based on the OTTDP-based HBF scheme, the deployment of plentiful AAUs is low-cost and low-complexity. The performance degradations due to the limited feedback precoding are analyzed in the next paragraph.

Figure 4(a) shows the three-dimensional (3D) beam pattern formed by the $\boldsymbol{\Phi}$ computed via the AO algorithm [34, 35]. Meanwhile, Figures 4(b)–(d) illustrates the 3D beam patterns formed by the CQ-based $\boldsymbol{\Phi}$ obtained by using $\mathfrak{R}_{54}$, $\mathfrak{R}_{\mathrm{DFT}}$, and $\mathfrak{R}_{43}$, respectively. The performance degradations due to

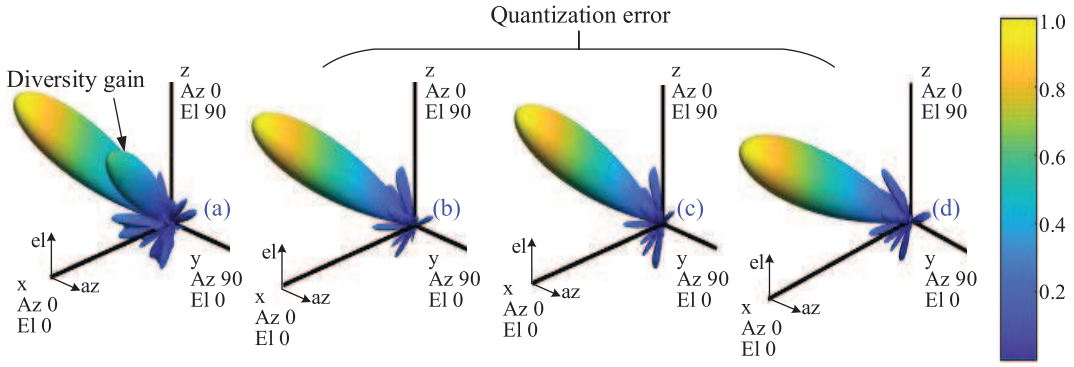

Figure 4 (Color online) Three-dimensional beam patterns formed by (a) the phase-shifting computed via the AO algorithm and the codebook-quantization-based phase-shifting by (b) $\mathfrak{R}_{54}$, (c) $\mathfrak{R}_{\mathrm{DFT}}$, and (d) $\mathfrak{R}_{43}$.

the limited feedback precoding can be attributed to two aspects. On the one hand, the CQ-based $\mathbf{\Phi}$ is unable to get diversity gain compared with the $\mathbf{\Phi}$ computed via the AO algorithm. On the other hand, the codebooks support finite beam patterns with discrete beampointing angles. Thus, a quantization error is also introduced into the limited feedback RIS-empowered mmWave C-RAN. From Figure 4, we can see that the beampointing angle based on the codeword generated from $\mathfrak{R}_{54}$ is closest to the beampointing angle of the beam pattern formed by the $\mathbf{\Phi}$ computed via the AO algorithm. In other words, the quantization error can be reduced by using a more precise codebook. As shown in Figure 3, better performance is achieved by using $\mathfrak{R}_{54}$ compared with that obtained by using $\mathfrak{R}_{43}$.

In the proposed NI-LF precoding for RIS-empowered mmWave C-RANs, the limited feedback hybrid precoding performed at each AAU is physically implemented by the OTTDP-based HBF in Subsection 2.2. The limited feedback of the analog precoding matrix is based on the codebook $\mathfrak{R}_\lambda$ determined by pre-designed OTTDP. In Figure 5, we compare the received SNR curves achieved by using $\mathfrak{R}_\lambda$ with different numbers of codewords, where the phase shift matrix of the RIS quantified by $\mathfrak{R}_{54}$ and $\mathfrak{R}_{\mathrm{DFT}}$ are respectively illustrated by the dotted line and the solid line. Specifically, we set the number of the codebooks to be ∞ ,12, 10, and 8, i.e., $K{=}\infty$, $K{=}12$, $K{=}10$, and $K{=}8$. Note that the codebook $\mathfrak{R}_\lambda$ with $K{=}\infty$ represents that the AAU uses unconstrained phase shifters to implement analog precoding. The corresponding results are marked by diamonds, squares, right-pointing triangles, and circles, as shown in Figure 5. For the RIS-empowered mmWave C-RAN, the received signal is combined with the signal directly sent by the AAU and that reflected by the RIS. When the user is located at $d_{\mathrm{h}} = 35$ m, the signals received from the AAU and the RIS are both weak due to the huge path losses at mmWave frequencies. As a result, we can see the curving around 35 m in Figure 5.

For the RIS-empowered mmWave C-RAN with OTTDP-based HBF, the difference between the received SNR curves obtained by the fully-digital precoding and the OTTDP-based HBF can be reduced by increasing the number of codewords in $\mathfrak{R}_\lambda$, as shown in Figure 5. However, for generating $\mathfrak{R}_\lambda$ with a larger number of codewords, the number of USOCs used to map the corresponding $\boldsymbol{M}_\lambda$ is also increased. Besides, the upper bound of the received SNR based on the OTTDP-based HBF is achieved by the codebook $\mathfrak{R}_\lambda$ with $K{=}\infty$, which is plotted in Figure 5 by diamonds. To balance performance and cost, therefore, we employ the OTTDP with 10 columns to perform analog precoding for the proposed RIS-empowered mmWave C-RAN with OTTDP-based HBF. The designed example of the $8{\times}10$ $\boldsymbol{M}_\lambda$ has been presented in Figure 2.

In Figure 6, we discuss the influence of the number of reflecting elements in the RIS, where all results are obtained from 5000 trials. Taking the phase-shifting quantified by $\mathfrak{R}_{\mathrm{DFT}}$ as an example, Figure 6(a) shows the case that the user is close to the location of the AAU, where $d_{\mathrm{h}} = 20$ m. In this case, the received SNR based on the AAU-RIS-MRT is worst since the signal component reflected by the RIS is weaker than that directly received from the AAU. With the increase of reflecting elements, the received SNR by the AAU-RIS-MRT also gets bigger. Because the received signal component directly from the AAU is dominant in the received SNR, the received SNR without the RIS is near-optimal. Further, the improvement generated from the increase of reflecting elements is slight. Correspondingly, Figure 6(b) shows the case that the user is close to the location of the RIS, where $d_{\mathrm{h}} = 50$ m. Due to huge path losses in mmWave frequencies, the signal from the AAU decays rapidly. Meanwhile, the signal reflected by the RIS is much stronger compared with that directly from the AAU. Therefore, the received SNR

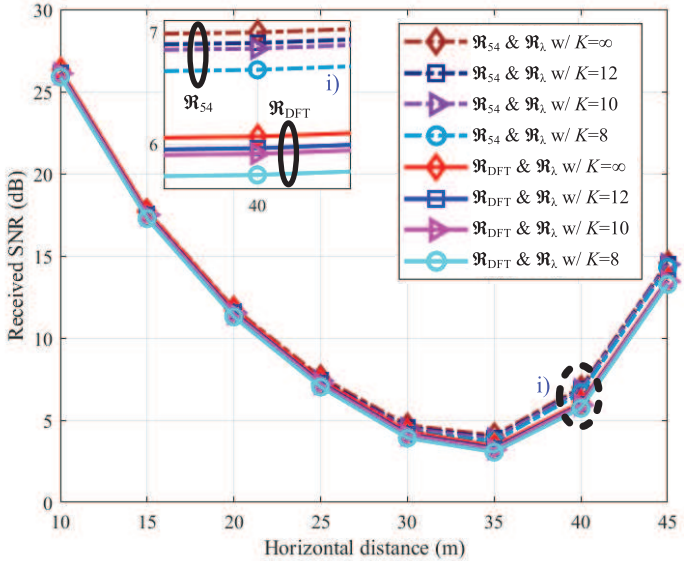

Figure 5 (Color online) Received SNR versus horizontal distance for $\mathfrak{R}_{\lambda}$ with $K = \infty$, $K = 12$, $K = 10$, and $K = 8$, where the phase-shifting is quantified by $\mathfrak{R}_{54}$ and $\mathfrak{R}_{\rm DFT}$.

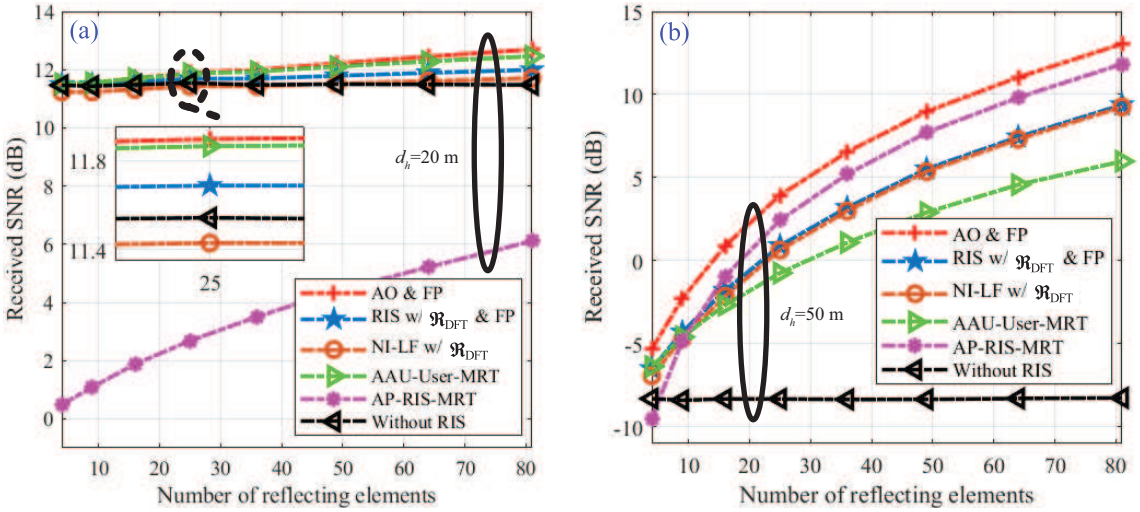

Figure 6 (Color online) Received SNR versus the number of reflecting elements at (a) $d_{\rm h} = 20$ m and (b) $d_{\rm h} = 50$ m.

empowered by the RIS is greatly improved and the performance obtained by the AAU-RIS-MRT becomes near-optimal. Compared with the mmWave C-RAN without the RIS, the RIS-empowered mmWave C-RAN with the OTTDP-based HBF and limited feedback archives much better performance. With the increase of reflecting elements, the 2D codebook $\mathfrak{R}_{\rm DFT}$ used in the NI-LF precoding algorithm is updated according to (11).

5 Conclusion

A novel OTTDP-based HBF has been proposed for the RIS-empowered mmWave C-RAN. Further, for the RIS-empowered mmWave C-RAN with OTTDP-based HBF, we developed a NI-LF precoding algorithm and then analyzed the computational complexity and overhead of the NI-LF precoding algorithm. For an AAU equipped with eight-element ULA, an example of the OTTDP with 10 beam patterns has been presented, where the beam modes supported by the OTTDP were plotted. Further, for a RIS-empowered mmWave C-RAN with 49 reflecting elements at 28 GHz, the received SNR via the developed NI-LF precoding algorithm was obtained, where the phase-shifting of RIS was quantified by $\mathfrak{R}_{54}$, $\mathfrak{R}_{\rm DFT}$, and $\mathfrak{R}_{43}$, respectively. The received SNR was compared with that via AO & FP, RIS w/ $\mathfrak{R}_{54}$ & FP, RIS w/

$\mathfrak{R}_{\mathrm{DFT}}$ & FP, and RIS w/ $\mathfrak{R}_{43}$ & FP, AAU-User-MRT, and AAU-RIS-MRT. The performance can be greatly improved based on the proposed NI-LF precoding compared with that via the precoding without RIS, especially for the user located near the RIS. Specifically, for the 49-element RIS, the proposed NI-LF precoding by using different codebooks to quantize the phase-shifting of the RIS respectively achieves 20.56, 19.55, and 18.93 dB performance improvement. Moreover, according to the 3D beam patterns of the phase-shift matrices computed by the AO algorithm and the CQ-based phase-shifting by $\mathfrak{R}_{54}$, $\mathfrak{R}_{\mathrm{DFT}}$, and $\mathfrak{R}_{43}$, performance degradations due to limited feedback were also analyzed. Moreover, we discussed the influence of the number of reflecting elements for different cases and the influence of the sizes of $\mathfrak{R}_{\lambda}$ mapped from the pre-designed OTTDP. The proposed OTTDP-based HBF and NI-LF precoding show a tremendous cost advantage for the RIS-empowered mmWave C-RAN, especially for the ultra-dense deployment of AAUs.

Acknowledgements This work was supported by National Key R&D Program of China (Grant No. 2018YFB1801302), Project for Zhongshan Social Public Welfare Science and Technology (Grant No. 2019B2007), and Project for Innovation Team of Guangdong University (Grant No. 2018KCXTD033).

References

1 Li X Y, Yu J J, Chang G K. Photonics-assisted technologies for extreme broadband 5G wireless communications. J Lightwave Technol, 2019, 37: 2851–2865
2 Lien S Y, Shieh S L, Huang Y, et al. 5G new radio: waveform, frame structure, multiple access, and initial access. IEEE Commun Mag, 2017, 55: 64–71
3 Kutty S, Sen D. Beamforming for millimeter wave communications: an inclusive survey. IEEE Commun Surv Tutorials, 2016, 18: 949–973
4 Zhang P, Yi C, Yang B S, et al. In-building coverage of millimeter-wave wireless networks from channel measurement and modeling perspectives. Sci China Inf Sci, 2020, 63: 180301
5 Bai T, Heath J R W. Coverage and rate analysis for millimeter-wave cellular networks. IEEE Trans Wireless Commun, 2015, 14: 1100–1114
6 Li L M, Wang D M, Niu X K, et al. mmWave communications for 5G: implementation challenges and advances. Sci China Inf Sci, 2018, 61: 021301
7 Sung M, Kim J, Kim E S, et al. RoF-based radio access network for 5G mobile communication systems in 28 GHz millimeter-wave. J Lightwave Technol, 2020, 38: 409–420
8 Kalfas G, Vagionas C, Antonopoulos A, et al. Next generation fiber-wireless fronthaul for 5G mmWave networks. IEEE Commun Mag, 2019, 57: 138–144
9 Alimi I A, Teixeira A L, Monteiro P P. Toward an efficient C-RAN optical fronthaul for the future networks: a tutorial on technologies, requirements, challenges, and solutions. IEEE Commun Surv Tut, 2018, 20: 708–769
10 Li C G, Song K, Wang D M, et al. Optimal remote radio head selection for cloud radio access networks. Sci China Inf Sci, 2016, 59: 102315
11 Wu C Y, Li H, Caytan O, et al. Distributed multi-user MIMO transmission using real-time sigma-delta-over-fiber for next generation fronthaul interface. J Lightwave Technol, 2020, 38: 705–713
12 Wu C Y, Li H, van Kerrebrouck J, et al. Distributed antenna system using sigma-delta intermediate-frequency-over-fiber for frequency bands above 24 GHz. J Lightwave Technol, 2020, 38: 2765–2773
13 Sohrabi F, Yu W. Hybrid digital and analog beamforming design for large-scale antenna arrays. IEEE J Sel Top Signal Process, 2016, 10: 501–513
14 Ayach O E, Rajagopal S, Abu-Surra S, et al. Spatially sparse precoding in millimeter wave MIMO systems. IEEE Trans Wireless Commun, 2014, 13: 1499–1513
15 Ye X, Zhang F, Pan S. Optical true time delay unit for multi-beamforming. Opt Express, 2015, 23: 10002–10008
16 Combi L, Spagnolini U. Adaptive optical processing for wideband hybrid beamforming. IEEE Trans Commun, 2019, 67: 4967–4979
17 Perez-Lopez D, Sanchez E, Capmany J. Programmable true time delay lines using integrated waveguide meshes. J Lightwave Technol, 2018, 36: 4591–4601
18 Blais S, Yao J. Photonic true-time delay beamforming based on superstructured fiber bragg gratings with linearly increasing equivalent chirps. J Lightwave Technol, 2009, 27: 1147–1154
19 Yang D H, Lin W P. Phased-array beam steering using optical true time delay technique. Optics Commun, 2015, 350: 90–96
20 Love D J, Heath J R N. Lau V K N, et al. An overview of limited feedback in wireless communication systems. IEEE J Sel Areas Commun, 2008, 26: 1341–1365
21 Xu D Y, Ren P Y, Du Q H, et al. Towards win-win: weighted-Voronoi-diagram based channel quantization for security enhancement in downlink cloud-RAN with limited CSI feedback. Sci China Inf Sci, 2017, 60: 040303
22 Alkhateeb A, Leus G, Heath J R W. Limited feedback hybrid precoding for multi-user millimeter wave systems. IEEE Trans Wireless Commun, 2015, 14: 6481–6494
23 Ayach O E, Rajagopal S, Abu-Surra S, et al. Limited feedback hybrid beamforming for multi-mode transmission in wideband millimeter wave channel. IEEE Trans Wireless Commun, 2020, 19: 4008–4022
24 Wang J Y, Lan Z, Pyo C-W, et al. Beam codebook based beamforming protocol for multi-Gbps millimeter-wave WPAN systems. IEEE J Sel Areas Commun, 2009, 27: 1390–1399
25 Han Y, Jin S, Zhang J, et al. DFT-based hybrid beamforming multiuser systems: rate analysis and beam selection. IEEE J Sel Top Signal Process, 2018, 12: 514–528
26 Bantavis P I, Kolitsidas C I, Empliouk T, et al. A cost-effective wideband switched beam antenna system for a small cell base station. IEEE Trans Antenn Propagat, 2018, 66: 6851–6861
27 Huang H, Zhang C F, Chen C, et al. Optical true time delay pools based centralized beamforming control for wireless base stations phased-array antennas. J Lightwave Technol, 2018, 36: 3693–3699
28 Huang H, Zhang C F, Yang C A, et al. Optical true time delay pool based hybrid beamformer enabling centralized beamforming control in millimeter-wave C-RAN systems. Sci China Inf Sci, 2020. doi: 10.1007/s11432-020-2991-1

29 Gong S, Lu X, Hoang D T, et al. Toward smart wireless communications via intelligent reflecting surfaces: a contemporary survey. IEEE Commun Surv Tut, 2020, 22: 2283–2314
30 Guo H, Liang Y C, Chen J, et al. Weighted sum-rate maximization for reconfigurable intelligent surface aided wireless networks. IEEE Trans Wireless Commun, 2020, 19: 3064–3076
31 Huang C, Zappone A, Alexandropoulos G C, et al. Reconfigurable intelligent surfaces for energy efficiency in wireless communication. IEEE Trans Wireless Commun, 2019, 18: 4157–4170
32 Wang Z, Shi Y, Zhou Y, et al. Wireless-powered over-the-air computation in intelligent reflecting surface-aided IoT networks. IEEE Internet Things J, 2021, 8: 1585–1598
33 Wu Q, Zhang R. Towards smart and reconfigurable environment: intelligent reflecting surface aided wireless network. IEEE Commun Mag, 2020, 58: 106–112
34 Wu Q, Zhang R. Intelligent reflecting surface enhanced wireless network: joint active and passive beamforming design. In: Proceedings of IEEE Global Communications Conference, United Arab Emirates, 2018. 1–6
35 Wu Q, Zhang R. Intelligent reflecting surface enhanced wireless network via joint active and passive beamforming. IEEE Trans Wireless Commun, 2019, 18: 5394–5409
36 Yang M C, Huang H, Zhang C F, et al. Optical codebook-based hybrid precoding for intelligent reflecting surface-assisted mmWave C-RAN systems. In: Proceedings of Asia Communications and Photonics Conference, Beijing, 2020. 336
37 Pradhan C, Li A, Song L, et al. Hybrid precoding design for reconfigurable intelligent surface aided mmWave communication systems. IEEE Wireless Commun Lett, 2020, 9: 1041–1045
38 Shi Y, Zhang J, Letaief K B. Group sparse beamforming for green cloud-RAN. IEEE Trans Wireless Commun, 2014, 13: 2809–2823
39 Wang Q, Zhou F, Hu R Q, et al. Energy efficient robust beamforming and cooperative jamming design for IRS-assisted MISO networks. IEEE Trans Wireless Commun, 2021, 20: 2592–2607
40 Zhou F, Li Z, Cheng J, et al. Robust AN-aided beamforming and power splitting design for secure MISO cognitive radio with SWIPT. IEEE Trans Wireless Commun, 2017, 16: 2450–2464
41 Dai L, Wang B, Peng M, et al. Hybrid precoding-based millimeter-wave massive MIMO-NOMA with simultaneous wireless information and power transfer. IEEE J Sel Areas Commun, 2019, 37: 131–141
42 Lu X, Yang W, Guan X, et al. Robust and secure beamforming for intelligent reflecting surface aided mmWave MISO systems. IEEE Wireless Commun Lett, 2020, 9: 2068–2072
43 Chae C-B, Mazzarese D, Jindal N, et al. A low complexity linear multiuser MIMO beamforming system with limited feedback. In: Proceedings of the 42nd Annual Conference on Information Sciences and Systems, Princeton, 2008. 418–422
44 Björnson E, Jorswieck E. Optimal resource allocation in coordinated multi-cell systems. Found Trends Commun Inf Theor, 2013, 9: 173–234
45 Liu H, Yuan X, Zhang Y J A. Matrix-calibration-based cascaded channel estimation for reconfigurable intelligent surface assisted multiuser MIMO. IEEE J Sel Areas Commun, 2020, 38: 2621–2636
46 Jung M, Saad W, Kong G. Performance analysis of active large intelligent surfaces (LISs): uplink spectral efficiency and pilot training. IEEE Trans Commun, 2021. doi: 10.1109/TCOMM.2021.3056532